

# Automatic Tissue Traction with Haptics-Enabled Forceps for Minimally Invasive Surgery

Tangyou Liu, *Graduate Student Member, IEEE*, Xiaoyi Wang, Jay Katupitiya, Jiaole Wang\*, *Member, IEEE*, and Liao Wu\*, *Member, IEEE*

**Abstract**—A common limitation of autonomous tissue manipulation in robotic minimally invasive surgery (MIS) is the absence of force sensing and control at the tool level. Recently, our team has developed haptics-enabled forceps that can simultaneously measure the grasping and pulling forces during tissue manipulation. Based on this design, here we further present a method to automate tissue traction with controlled grasping and pulling forces. Specifically, the grasping stage relies on a controlled grasping force, while the pulling stage is under the guidance of a controlled pulling force. Notably, during the pulling process, the simultaneous control of both grasping and pulling forces is also enabled for more precise tissue traction, achieved through force decoupling. The force controller is built upon a static model of tissue manipulation, considering the interaction between the haptics-enabled forceps and soft tissue. The efficacy of this force control approach is validated through a series of experiments comparing targeted, estimated, and actual reference forces. To verify the feasibility of the proposed method in surgical applications, various tissue resections are conducted on *ex vivo* tissues employing a dual-arm robotic setup. Finally, we discuss the benefits of multi-force control in tissue traction, evidenced through comparative analyses of various *ex vivo* tissue resections. The results affirm the feasibility of implementing automatic tissue traction using micro-sized forceps with multi-force control, suggesting its potential to promote autonomous MIS. A video demonstrating the experiments can be found at <https://youtu.be/8fe8o81FrjE>.

**Index Terms**—Minimally invasive surgery, surgical robots, haptics-enabled forceps, automatic tissue traction, grasping and pulling force control.

## I. INTRODUCTION

**S**URGICAL robots equipped with miniature instruments have been extensively studied in recent years, demonstrating significant potential for minimally invasive surgery (MIS) [1]–[6]. Within this field, micro-sized forceps are increasingly employed for precise tissue manipulation [7]–[13]. In addition, as surgical robots advance towards enhanced autonomy, the

importance of precise robotic tissue manipulation is increasingly recognized [1], [14]. To facilitate efficient and safe tissue manipulation in robotic MIS, precise control over the grasping and pulling forces exerted by micro-sized forceps is vital, which is amplified by the potential of severe complications associated with improper manipulation forces [15]–[18]. However, this crucial functionality remains absent in most systems employing miniature instruments.

Tissue traction, comprising grasping and pulling, is a frequently performed surgical task [17]. For example, Fig.1(a) illustrates a robotic thyroidectomy scenario, adapted from [17], where forceps and scissors collaboratively undertake cyst dissection. During such procedures, the traction executed by the forceps necessitates both separate and simultaneous control of grasping and pulling forces. This control is crucial to prevent tissue damage and ensure optimal surgical outcomes, as shown in Fig.1(b)–(e). In particular, grasping and pulling forces are highly coupled during the tissue pulling process, and they are significantly influenced by the interaction between instrument and tissue [19]–[21]. In response to the need for enhanced precision in robotic surgery, this paper introduces a method for automatic tissue traction using micro-sized forceps featuring controlled forces.

An extensively studied approach enabling force control in tissue manipulation involves observing and controlling tissue deformation, which often relies on imaging techniques [22]. For instance, Haouchine *et al.* [23] utilized endoscopic images to develop an underlying biomechanical model for estimating and controlling contact force. Beyond tissue modeling, research has also explored learning methods for estimating and controlling interaction forces using visual information. Lee *et al.* [24] achieved contact force estimation and control using a neural network-based method, integrating actuators' electrical current and camera images to enhance accuracy. Nevertheless, these learning-based approaches often require complex training processes and present practical challenges in surgical settings due to the need for extensive preparation [1], [22], [25]. Moreover, the reliability of these methods depends on precise, real-time modeling of tissue biomechanical properties, posing significant challenges in robustness and applicability in diverse surgical scenarios [26].

In addition to monitoring tissue deformation, numerous studies have concentrated on developing force sensing and control directly at the tool level. For example, Xiang *et al.* [27] employed a learning-based approach to facilitate contact force estimation and control at the continuum robot's tip. While the training of the neural networks involved only the actuator's

Research was partly supported by Australian Research Council under Grant DP210100879, Heart Foundation under Vanguard Grant 106988, and UNSW Engineering under GROW Grant PS69063 awarded to Liao Wu, partly by the Talent Recruitment Project of Guangdong under Grant 211223808012 and the Science and Technology Innovation Committee of Shenzhen under Grant JCYJ20220818102408018 awarded to Jiaole Wang, and partly by the Tyree IHealthE PhD Top-Up Scholarship and China Scholarship Council PhD Scholarship awarded to Tangyou Liu. \*Corresponding authors: Jiaole Wang ([wangjiaole@hit.edu.cn](mailto:wangjiaole@hit.edu.cn)) and Liao Wu ([liao.wu@unsw.edu.au](mailto:liao.wu@unsw.edu.au)).

Tangyou Liu, Jay Katupitiya, and Liao Wu are with the School of Mechanical & Manufacturing Engineering, University of New South Wales, Sydney, NSW 2052, Australia.

Xiaoyi Wang is with the School of Electrical Engineering and Telecommunications, University of New South Wales, Sydney, NSW 2052, Australia.

Jiaole Wang is with the School of Mechanical Engineering and Automation, Harbin Institute of Technology, Shenzhen, 518055, China.

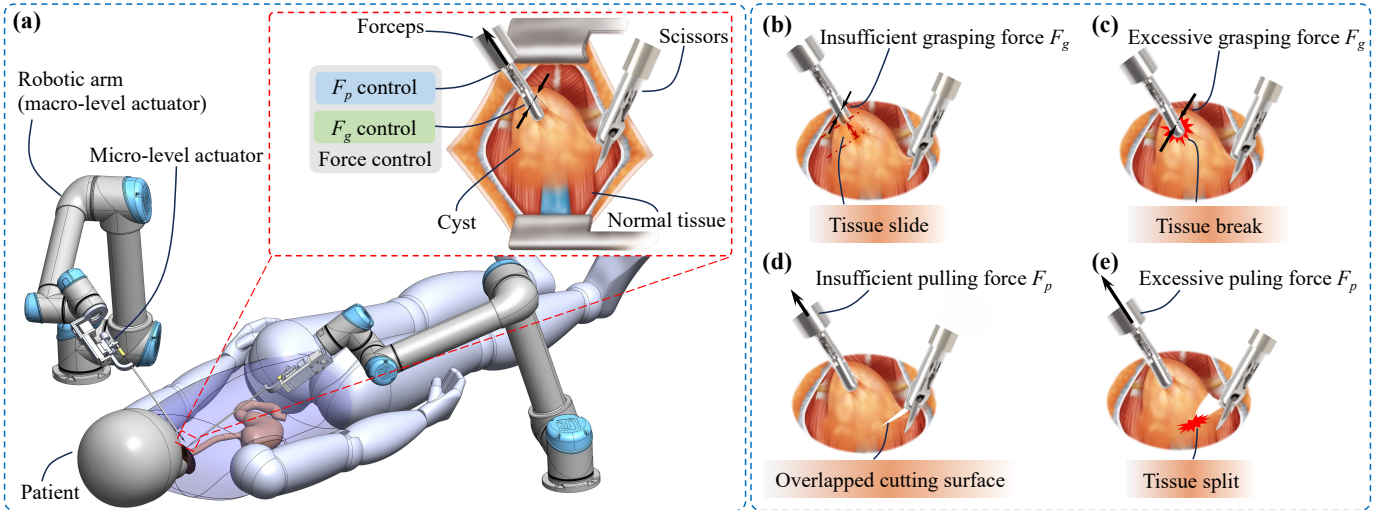


Fig. 1. Typical tissue resection with forceps and scissors. (a) Dual-arm robotic system for lesion resection, where the forceps are responsible for tissue traction, while the scissors are responsible for tissue cutting (inset is adapted from [17]). The grasping force  $F_g$  control and pulling force  $F_p$  control are crucial for efficient and safe tissue traction. (b) and (c) show tissue slide and break results from insufficient and excessive grasping forces  $F_g$ , respectively. (d) insufficient tissue pulling force  $F_p$  results in cutting surface overlapping and prevents the scissors from performing continuous cuts. (e) unexpected tissue split results from excessive pulling force  $F_p$ .

state and a reference contact force, the implementation phase necessitated prior biomechanical information. Alternatively, Wijayarathne *et al.* [28] developed a model for detecting contact in force-modulated manipulation, using Yong’s modules of both tooltip and contact surface. In contrast, Sheng *et al.* [29] bypassed the need for intricate modeling by directly affixing a force sensor at the instrument’s base, enabling control of the instrument-tissue contact force. This approach was complemented by a vision system to guide the instrument’s desired orientation.

Specifically for surgical forceps, several studies have facilitated force sensing by adapting and installing sensors into the forceps’ jaws, as demonstrated in [20], [30], [31]. Despite these advancements, effective control of the forceps’ grasping or pulling forces remains largely unexplored, particularly regarding their simultaneous control. The considerable size of these sensing modules, along with the modifications required on the jaws, impedes their integration into micro-sized forceps, such as those adopted in [7]–[12]. Additionally, it is challenging to visually monitor and measure tissue deformation with such small forceps, especially between the two jaws, for estimating and controlling grasping forces [32].

In summary, while the aforementioned studies achieved contact or grasping force control, they do not apply to micro-sized forceps, and none of them have accomplished simultaneous multi-force control, a more challenging task that involves force coupling. In our previous work [21], we introduced a vision-based module that achieved multi-modal force sensing in micro-sized forceps, including grasping and pulling forces. This paper extends our previous investigation to explore automatic tissue traction with micro-sized forceps featuring decoupled control of multiple forces.

The main contribution of this work is the proposal of a method for automatic tissue traction featuring controlled

grasping and pulling forces using micro-sized forceps. Specifically, the grasping stage relies on a controlled grasping force, while the pulling stage is under the guidance of a controlled pulling force, as depicted in Fig. 1(a). Notably, during the pulling process, the simultaneous control of both grasping and pulling forces is also enabled for more precise tissue traction, achieved through force decoupling. The force controller is designed based on a static model of tissue manipulation that considers the interaction between forceps and soft tissues. The efficacy of the proposed controller is validated through a series of experiments comparing the target, estimated, and reference results. Further integrating these haptics-enabled forceps in a dual-arm robotic system, we demonstrate the potential surgical application of the automatic tissue traction by a series of resections on *ex vivo* tissue. Finally, we discuss the benefits of multi-force control in tissue traction, evidenced through comparative analyses of various *ex vivo* tissue resections.

## II. SYSTEM DESCRIPTION AND MODELING

### A. Haptics-Enabled Forceps and Force Sensing

Haptics-enabled forceps and their vision-based force estimation method have been presented in our previous work [21]. Integrated with a micro-level actuator, the efficacy of this new kind of micro-sized forceps has been validated for force estimation in robotic tissue manipulation tasks. To reduce duplication without compromising comprehensibility, we briefly describe the current prototype. Subsequently, we clarify how the driving force and supporting force applied to the forceps are independently estimated, followed by the calculation of pushing/pulling force and grasping force.

The micro-level actuator (Fig. 2(a) is optimized by a portable design considering sterilization and delivery. The instrument integrated with the haptics-enabled forceps (Fig. 2(b) shows the prototype) can achieve one-step mating with the

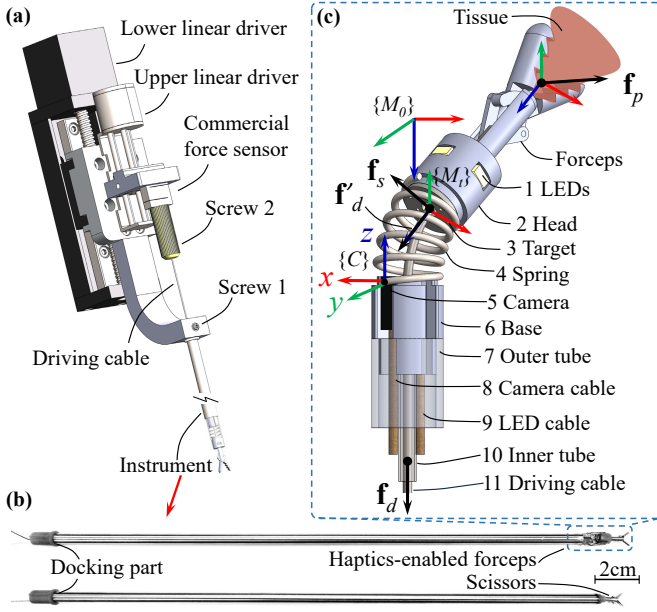


Fig. 2. Portable instruments and micro-level actuator. (a) The micro-level actuator updated from [21], wherein the screw 1 is used to fix the instrument's stainless tube, and the screw 2 is used to lock the forceps' driving cable. (b) Instrument prototypes that integrate with the haptics-enabled forceps and scissors, wherein the docking part positions and orientates the instrument. (c) Haptics-enabled forceps with a vision-based force sensing module presented in [21], where the camera (5) is used to measure the deformation of the spring (4) by tracking and estimating the pose of the target (3). An inner tube (10) is installed concentrically to the outer stainless tube (7) to pass through the forceps' driving cable (11) only. The driving force  $\mathbf{f}_d$  applied on the cable is measured by the proximal commercial force sensor.  $\mathbf{f}'_d$  denotes the effective driving force transmitted to the forceps' jaws through the central cable.  $\mathbf{f}_s$  is the supporting force from the sensing module, and  $\mathbf{f}_p$  is the pushing/pulling force from the tissue.

micro-level actuator through a docking part and then be fixed by two screws. To avoid interference from the camera and LED cables, an inner tube is concentrically installed along with the outer stainless tube to enclose the forceps' driving cable only, as shown in Fig. 2(c).

The forces applied to the forceps when they push or pull a tissue are also shown in Fig. 2(c).  $\mathbf{f}_d$  is the driving force from the cable,  $\mathbf{f}_p$  is the pushing/pulling force from the interactive tissue, and  $\mathbf{f}_s$  is the supporting force applied to the forceps' base from the installed sensing module. The driving force  $\mathbf{f}_d$  is directly measured by a commercial gauge force sensor installed at the proximal end of the instrument shown in Fig. 2(a). However, estimating the supporting force  $\mathbf{f}_s$  is more challenging as it is located at the tip side, which is realized by our vision-based sensing module. Since the supporting force  $\mathbf{f}_s$  is equal to the elastic force from the spring, it can be formulated as

$$\mathbf{f}_s = \mathbf{K}_s \mathbf{t}_s, \quad (1)$$

where  $\mathbf{K}_s$  is the spring's stiffness matrix,  $\mathbf{t}_s$  is the translation vector of  ${}^{M_0}\mathbf{T}$ , representing the spring's deformation, and estimated by the sensing module's camera by tracking the installed target. Because the estimation of  $\mathbf{f}_s$  solely depends on the spring's deformation, it can be directly and independently estimated by the vision-based sensing module. Consequently, this allows for the driving force  $\mathbf{f}_d$  and supporting force  $\mathbf{f}_s$

applied to the forceps to be measured independently and concurrently.

According to the force equilibrium, the pulling force  $\mathbf{f}_p$  can be obtained by

$$\mathbf{f}_p = -\frac{M_0}{M_t} \mathbf{T} \mathbf{f}_d - \mathbf{f}_s. \quad (2)$$

On the other hand, associating with the estimated driving force  $\mathbf{f}_d$ , supporting force  $\mathbf{f}_s$ , and the forceps' geometry, the grasping force can also be obtained. Fig. 3(a) shows the sectional view of the forceps and forces applied to them when grasping and pulling tissue, and the lower-left inset shows the corresponding forces applied to the grasped tissue. We define the contact force between the tissue and forceps' jaws as the grasping force  $F_g$ . For convenience, we adopt  $F_\bullet$  and  $t_\bullet$  to denote the magnitude of force  $\mathbf{f}_\bullet$  and displacement  $\mathbf{t}_\bullet$  in the following sections. For a pair of forceps, we assume  $F_{g1}$  equals  $F_{g2}$ , and  $F_{f1}$  equals  $F_{f2}$ . Then, referring to the lower-right inset in Fig. 3(a), we can formulate  $F_g$  by  $F_d$  as

$$F_g = \frac{F_d l_2 \sin \alpha}{2l_3}, \quad (3)$$

where  $\alpha = \frac{\theta}{2} + \alpha_0$ , and the definitions of  $\theta$ ,  $\alpha$ ,  $\alpha_0$ ,  $l_2$  and  $l_3$  are shown in Fig. 3(b).

Moreover, according to the relationship of forceps' links at the initial state (the left of Fig. 3(b)), we can get  $\alpha_0$  by

$$\alpha_0 = \arccos \frac{l_{1,2}^2 + l_2^2 - l_1^2}{2l_1 l_{1,2}}, \quad (4)$$

where  $l_{1,2}$  is the distance between forceps' two joints  $j_1$  and  $j_2$ . The right sub-figure of Fig. 3(b) shows the geometry when the forceps are opened at an angle of  $\theta$ . In this state, the angle  $\alpha$  can be calculated as

$$\alpha = \arccos \frac{l'_{1,2}{}^2 + l_2^2 - l_1^2}{2l_1 l'_{1,2}}, \quad (5)$$

where  $l'_{1,2} = l_{1,2} + t_d - t_s$ ,  $t_d$  is the displacement of the driving cable measured by the upper driver's encoder of the micro-level actuator, and  $t_s$  is the displacement of the sensor's head estimated by the embedded camera.

### B. Model of Tissue Traction with Forceps

Haptics-enabled forceps paved the way for tissue manipulation, including controlling the grasping force  $F_g$  and the pulling force  $F_p$ . To facilitate efficient and safe robotic tissue traction, it is essential to control these multiple forces applied to the tissue.

Although a tissue could be ideally modelled by a Voigt-Kelvin model [26], the specific characteristics of different tissues are various and complex. Here, we simplify the grasped tissue by a model that consists of a viscous damper  $c_t$  and elastic spring  $k_t$  for the mathematical model derivation. Assuming the forceps grasp the tissue stably and there is no slide or tissue breaking, we introduce a static model when the haptics-enabled forceps grasp and pull the tissue as shown in Fig. 3(c).

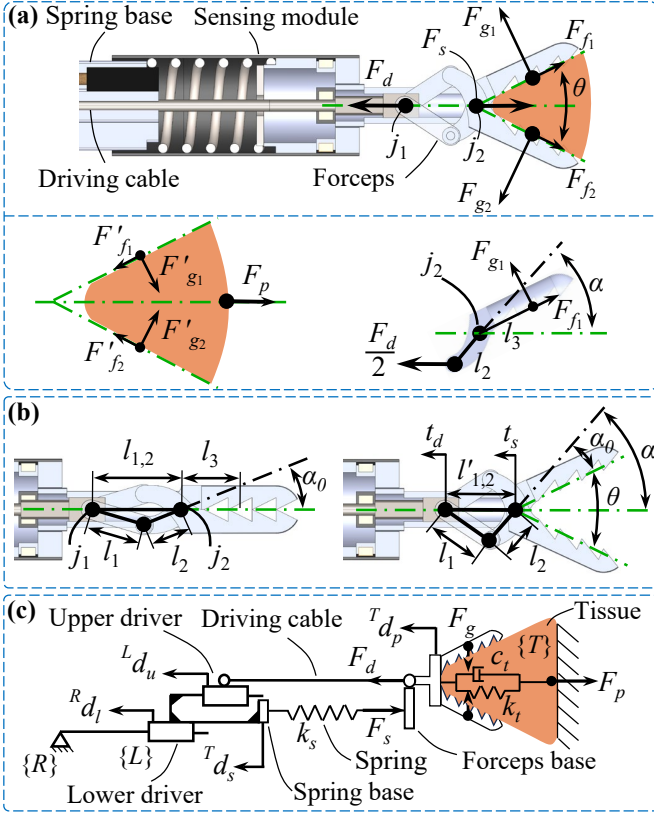


Fig. 3. (a) Forces applied to the forceps when they grasp and pull a tissue include driving force  $F_d$  from the cable, supporting force  $F_s$  from the sensing module, contact force  $F_g$  (also called grasping force), and friction force  $F_f$  from the tissue. The left inset shows the forces applied to the grasped tissue, where  $F_p$  is the pulling force from the tissue body,  $F'_g = F_g$  and  $F'_f = F_f$  are forces from the forceps. The right inset shows the forces that generate the momentum of one jaw about joint  $j_2$ .  $F_d$  is measured by the proximal force sensor. (b) Sectional views of the haptics-enabled forceps when the two jaws are closed (left) and open at  $\theta$  (right).  $t_d$  is the transformation of the driving cable measured by the upper driver's encoder of the micro-level actuator, while  $t_s$  is the transformation of the sensing module's head estimated by the sensing module's camera. (c) Model of tissue traction with haptics-enabled forceps.  $T_d_p$  and  $T_d_s$  denote the displacement of the forceps' jaws related to the tissue body  $\{T\}$  and that of the spring base related to  $\{T\}$ , respectively.  $R_d_l$  is the lower driver displacement associated with its mounting points on the robotic arm  $\{R\}$ , while  $L_d_u$  is the upper driver displacement related to its mounting points on the lower driver  $\{L\}$ .

The system has two inputs  $\mathbf{u} = [u_1, u_2]^\top = [{}^R d_l, {}^L d_u]^\top$ , and two outputs  $\mathbf{y} = [y_1, y_2]^\top = [F_g, F_p]^\top$ . According to Fig. 3(c), we have below two function groups:

$$\begin{cases} F_d = k_t T d_p + c_t \dot{T} d_p + k_s (T d_p - T d_s) \\ F_p = k_t T d_p + c_t \dot{T} d_p \end{cases}, \quad (6)$$

where  $T d_p - T d_s = T t_s$ ,  $T d_p$  and  $T d_s$  denote the displacement of the forceps' jaws related to the tissue body  $\{T\}$  and that of the spring base related to  $\{T\}$ .

$$\begin{cases} T d_p = R d_l + L d_u \\ T d_s = R d_l \end{cases}, \quad (7)$$

where  $R d_l$  is the lower driver displacement related to its mounting point on the robotic arm  $\{R\}$ , while  $L d_u$  is the upper driver displacement related to its mounting point on the lower driver  $\{L\}$ .

Then, defining the state variables as  $\mathbf{x} = [x_1, x_2]^\top = [T d_p, T d_s]^\top$ , we can formulate the state-space equations as

$$\dot{\mathbf{x}} = \mathbf{A}\mathbf{x} + \mathbf{B}\mathbf{u}, \quad (8)$$

with  $\mathbf{A} = \mathbf{0}$  and  $\mathbf{B} = \begin{bmatrix} 1 & 1 \\ 1 & 0 \end{bmatrix}$ .

Referring to (3), (6), and (7), we can obtain the outputs as

$$\mathbf{y} = \mathbf{C}\mathbf{x} + \mathbf{D}\mathbf{u}, \quad (9)$$

where

$$\mathbf{C} = \begin{bmatrix} \frac{l_2 \sin \alpha}{2l_3} (k_t + k_s) & -\frac{l_2 \sin \alpha}{2l_3} k_s \\ k_t & 0 \end{bmatrix}, \mathbf{D} = \begin{bmatrix} \frac{l_2 \sin \alpha}{2l_3} c_t & \frac{l_2 \sin \alpha}{2l_3} c_t \\ c_t & c_t \end{bmatrix}.$$

Because  $\text{rank}([\mathbf{B}, \mathbf{A}\mathbf{B}]) = 2$  and  $\text{rank}([\mathbf{C}^\top, \mathbf{A}^\top \mathbf{C}^\top]^\top) = 2$ , the system is both controllable and observable.

### III. METHODS FOR AUTOMATIC TISSUE TRACTION

To achieve precise and automatic tissue traction, the forceps must be capable of following predefined grasping and pulling force profiles. Consequently, it becomes essential to design controllers for grasping and pulling processes. However, it is challenging to model tissue mechanical properties precisely in real time, and the controller needs to be adaptive to deal with various tissues. Here, we adopt a standard and effective proportional–integral–derivative (PID) controller to enable the forceps to track these force profiles,

$$u(t) = K_P e(t) + K_I \int_0^t e(\tau) d\tau + K_D \dot{e}(t), \quad (10)$$

where  $e(t) = F_\bullet^*(t) - F_\bullet^e(t)$  is the error between the observed force  $F_\bullet^e(t)$  and the target value  $F_\bullet^*(t)$ , and  $\bullet$  denotes subscript  $\{g, p\}$  for grasping and pulling forces, respectively.

#### A. Tissue Grasping with Controlled $F_g$

1) *Controller Design*: In our haptics-enabled forceps, the current  $F_g^e$  is estimated and observed in each running cycle via (3). Originally, we plan to apply a group of parameters  $[K_{P,1}, K_{I,1}, K_{D,1}]$  with controller (10) to control the grasping force  $F_g$ . However, from (3), we find that  $F_g$  is positively related to  $\theta$ . Therefore, we set the corresponding parameters  $[K_{P,1}^\theta, K_{I,1}^\theta, K_{D,1}^\theta]$  of different  $\theta$  configurations as below (11) to minimize the difference in response.

$$[K_{P,1}^\theta, K_{I,1}^\theta, K_{D,1}^\theta] = f(\theta) [K_{P,1}, K_{I,1}, K_{D,1}], \quad (11)$$

where  $f(\theta) = \frac{\sin \alpha_0}{\sin(\frac{\theta}{2} + \alpha_0)}$  is a function related to  $\theta$ .

In addition, considering the deformation of the spring and the press deformation of the tissue, we set the speed of the lower driver  ${}^R \dot{d}_l$  as

$${}^R \dot{d}_l(t) = -\frac{T t_s(t)}{L d_u(t)} L \dot{d}_u(t). \quad (12)$$

This can compensate for the elastic motion and minimize the forceps tip movement, i.e., keeping  $T d_p = 0$  by setting  ${}^R d_l(\tau) = -T t_s(\tau)$  with  $\int_0^t {}^R d_l(\tau) d\tau = -\int_0^t \frac{T t_s(\tau)}{L d_u(\tau)} L d_u(\tau) d\tau$ .

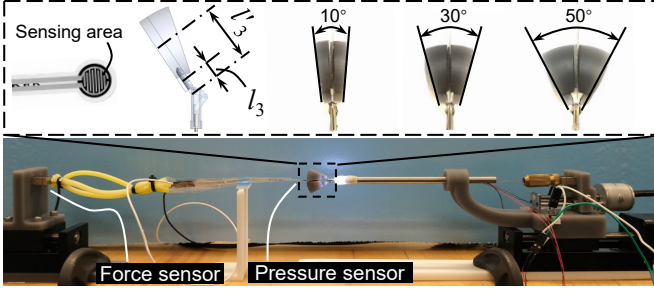


Fig. 4. Experimental setup for force control evaluation, where a commercial gauge force sensor and pressure sensor were adopted to measure references pulling and grasping forces, respectively. The inset shows three 3D-printed contact surfaces configured with  $\theta = 10^\circ$ ,  $30^\circ$ , and  $50^\circ$ .

Consequently, the input for the upper driver in the tissue grasping process with controlled  $F_g$  can be set as

$${}^L\dot{d}_u(t) = f(\theta)(K_{P,1}e_1(t) + K_{I,1}\int_0^t e_1(\tau)d\tau + K_{D,1}\dot{e}_1(t)), \quad (13)$$

where  $e_1(t) = F_g^*(t) - F_g^e(t)$ ,  $F_g^*(t)$  is the target grasping force, and  $F_g^e(t)$  is the current estimated grasping force.

2) *Experimental Evaluation*: Fig. 4 shows the experimental setup, where a commercial pressure sensor (RFP603 200g, RFP<sup>®</sup>, China), with a resolution of 0.01N, was adopted as reference. The forceps grasped the commercial pressure sensor, which directly measured the reference grasping force. Because the pressure sensor's sensing area was a 10mm-diameter circle, 3D-printed surfaces were attached to the forceps' jaws to ensure sufficient contact. Consequently,  $l_3$  in (3) was set as  $l'_3$  in the following experiments.

Because the grasping force is positively related to the grasping angle  $\theta$ , as shown in (3), the maximum grasping force that the forceps can produce varies with different  $\theta$ . Moreover, to cover the range of  $F_g$  estimation as much as possible, we set the amplitude of target grasping force profile  $F_g^*$  to 0.2N, 0.25N, and 0.3N for experiments with  $\theta = 10^\circ$ ,  $30^\circ$ , and  $50^\circ$ , respectively, and noted by  $i \in \{1, 2, 3\}$ . The frequency of  $F_g^*$  was set to 1/30Hz, 1/15Hz, and 1/10Hz and repeatedly applied to experiments with different  $\theta$  configurations.

Fig. 5(a), (b), and (c) show the grasping force results of experiments conducted with the targeted grasping force frequency equalled 1/30Hz, 1/15Hz, and 1/10Hz, respectively. For clarification, we plotted results with the same  $F_g^*$  frequency in the same subplot.  $F_{g,i}^*$ ,  $F_{g,i}^e$ , and  $F_{g,i}^r$  denote inputted target grasping force, forceps-estimated grasping force, and measured reference grasping force, respectively. Fig. 5(d) plots the errors between  $F_{g,i}^*$ ,  $F_{g,i}^e$ , and  $F_{g,i}^r$ . We also noticed that the error between  $F_{g,i}^*$  and  $F_{g,i}^e$  tended to increase when the frequency of the targeted force  $F_{g,i}^*$  increased, and the maximum error (0.095N) was observed in the experiment with 1/10Hz and  $\theta = 50^\circ$ . On the contrary, errors between  $F_{g,i}^*$  and  $F_{g,i}^e$  showed slight variations, yet all were below 0.06N. This indicates the grasping force  $F_g$  can be estimated and controlled effectively during the grasping process.

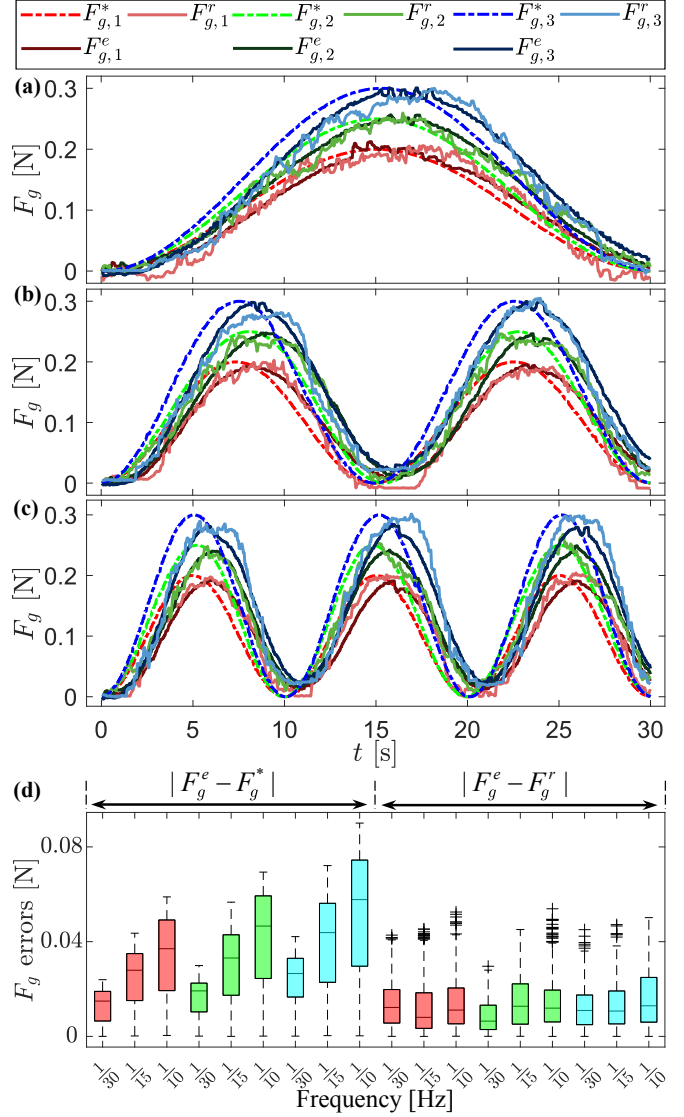


Fig. 5. Evaluation results of tissue grasping with controlled  $F_g$ . (a), (b), and (c) are results of experiments conducted with  $F_g^*$  frequency was set to 1/30Hz, 1/15Hz, and 1/10Hz, respectively.  $F_{g,i}^*$ ,  $F_{g,i}^e$ , and  $F_{g,i}^r$  indicate targeted, estimated, and reference grasping forces.  $i = 1, 2, 3$  indicate experiments conducted with grasping angle  $\theta = 10^\circ$ ,  $30^\circ$ ,  $50^\circ$ , and the corresponding amplitudes of  $F_{g,i}^*$  are 0.2N, 0.25N, and 0.3N. (d) Corresponding errors patched with red ( $i = 1$ ), green ( $i = 2$ ), and blue ( $i = 3$ ). The first nine boxes are the errors between  $F_{g,i}^e$  and  $F_{g,i}^*$ , while the last nine are the errors between  $F_{g,i}^e$  and  $F_{g,i}^r$ .

## B. Tissue Pulling with Controlled $F_p$

1) *Controller Design*: In our haptics-enabled forceps, the current  $F_p^e$  is also estimated and observed in each running cycle via (2). We assume the tissue has been grasped stably for the pulling stage, and the upper driver is locked by setting

$${}^L\dot{d}_u(t) = 0. \quad (14)$$

Then, the pulling force control can be achieved by directly relying on the lower driver's motion. Consequently, the input for the lower driver in the pulling process with controlled  $F_p$  can be set as

$${}^R\dot{d}_l(t) = K_{P,2}e_2(t) + K_{I,2}\int_0^t e_2(\tau)d\tau + K_{D,2}\dot{e}_2(t), \quad (15)$$

where  $e_2(t) = F_p^*(t) - F_p^e(t)$ ,  $F_p^*(t)$  is the target pulling force, and  $F_p^e(t)$  is the current estimated pulling force.

2) *Experimental Evaluation*: Similarly, we evaluate the pulling force control by actuating the forceps to follow a series of inputted force profiles  $F_p^*$  with different amplitudes and frequencies. The experimental setup is shown in Fig. 4, where the reference pulling force  $F_p^r$  is measured by a commercial gauge force sensor that is connected to the pressure sensor by a flexure. The forceps initially grasped the commercial pressure sensor with a grasping force  $F_g = 0.2N$ . Then, the forceps pulled the pressure sensor with inputted target pulling force profile  $F_p^*$ . The amplitude of  $F_p^*$  was 2.0N, while the frequency was set to 1/30Hz, 1/15Hz, and 1/10Hz. Each experiment was repeated with grasping angle  $\theta = 10^\circ, 30^\circ$ , and  $50^\circ$ , and noted by  $i \in (1, 2, 3)$ .

Fig. 6(a), (b), and (c) present the comparisons of pulling force  $F_p$  in experiments conducted with  $F_p^*$  frequency equals to 1/30Hz, 1/15Hz, and 1/10Hz, respectively. For clarification, we plotted results with the same  $F_p^*$  frequency in the same subplot.  $F_{p,i}^*$ ,  $F_{p,i}^e$ , and  $F_{p,i}^r$  denote inputted target pulling force, forceps estimated pulling force, and measured reference pulling force. Fig. 6(d) plots the errors between  $F_p^*$ ,  $F_p^e$ , and  $F_p^r$ . The error between  $F_p^*$  and  $F_p^e$  tended to increase when the frequency of  $F_p^*$  increased, and the maximum error 0.4N was observed in the experiment with 1/10Hz and  $\theta = 50^\circ$ . On the contrary, errors between  $F_p^e$  and  $F_p^r$  showed slight variations, yet all were below 0.2N. This indicates that  $F_p$  can be estimated and controlled efficiently during the pulling process.

### C. Tissue Traction with Controlled $F_g$ and $F_p$

#### 1) Integrated Controller for grasping and pulling stages:

The results above have shown the potential of the proposed controllers in automatic tissue traction, which consists of a grasping stage followed by a pulling stage. In particular, the grasping stage can directly employ the controller developed in Sec. III-A, i.e., pure grasping force control using (12) and (13).

The pulling stage may also just use the pure pulling force controller proposed in Sec. III-B; however, a notable coupling between  $F_p$  and  $F_g$  was observed in the experiments in Sec. III-B. For example, Fig. 7 presents the  $F_g$  variation resulting from changed  $F_p$  that corresponds to experiments in Fig. 6(a), and these variations were 0.073N, 0.096N, and 0.116N for  $\theta = 10^\circ, 30^\circ$ , and  $50^\circ$ , respectively. This force coupling phenomenon was also observed in [19]–[21] when these studies evaluated their forceps' force sensing capabilities.

The force coupling phenomenon can be explained by (2) and (3). Referring to them, we can formulate grasping force as

$$F_g = \frac{F_d l_2 \sin \alpha}{2l_3} = \frac{(F_p + F_s) l_2 \sin \alpha}{2l_3}, \quad (16)$$

where  $F_d = F_p + F_s$ . This indicates that the grasping force  $F_g$  is positively related to the pulling force  $F_p$ .

When dealing with delicate and critical tissues, it is often desirable to maintain a controlled grasping force while pulling the tissue. Therefore, we propose to simultaneously control the grasping and pulling forces during the tissue pulling stage.

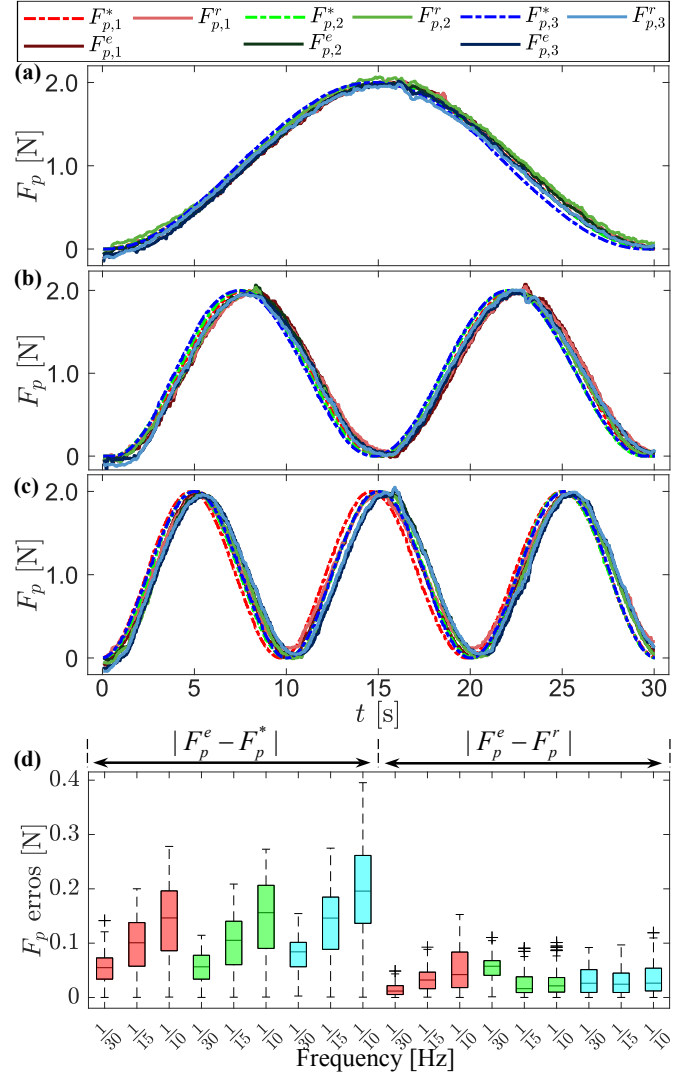


Fig. 6. Evaluation results of tissue pulling with controlled  $F_p$ . (a), (b), and (c) present results of experiments conducted with  $F_p^*$  frequency was set to 1/30Hz, 1/15Hz, and 1/10Hz, respectively, and the amplitude was 2.0N.  $F_p^*$  and  $F_{g,i}^*$  denote targeted pulling and grasping forces.  $F_{p,i}^e$  and  $F_{g,i}^e$  are the estimated forces by the haptics-enabled forceps, while  $F_{p,i}^r$  and  $F_{g,i}^r$  are reference forces measured by commercial sensors.  $i \in (1, 2, 3)$  denotes experiment conducted with grasping angle  $\theta = 10^\circ, 30^\circ$ , and  $50^\circ$ . (d) Corresponding errors patched with red ( $i = 1$ ), green ( $i = 2$ ), and blue ( $i = 3$ ). The first nine boxes are the errors between  $F_p^e$  and  $F_p^*$ , while the last nine are those between  $F_p^e$  and  $F_p^r$ .

This can be conveniently achieved by setting the inputs for lower and upper drivers in the pulling process with (15) and (13), respectively.

2) *Experimental Evaluation*: Here, we adopted the same experimental setup shown in Fig. 4. The experimental procedures simulated the tissue traction process with the following considerations. First, the forceps grasp the pressure sensor following a target grasping force profile  $F_g^*$ . Then, during the pulling process, the forceps pull the pressure sensor following a target pulling force profile  $F_p^*$  while keeping the grasping force in a constant value  $F_g^{*,t}$ .  $F_g^{*,t}$  simulated a threshold to limit the grasping force and avoid unexpected tissue breaking.

Specifically, the targeted grasping force  $F_g^*$  first gradually increased from zero to the threshold  $F_g^{*,t} = 0.2N$  during the

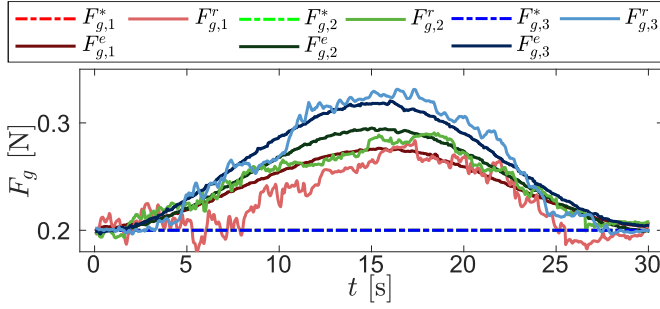


Fig. 7. Grasping force  $F_g$  variation resulting from coupling with pulling force  $F_p$ .  $F_{g,i}^*$ ,  $F_{g,i}^e$ , and  $F_{g,i}^r$  indicate targeted, estimated, and reference grasping forces.  $i = 1, 2$ , and  $3$ , indicates experiments conducted with grasping angle  $\theta = 10^\circ, 30^\circ, 50^\circ$ . In these experiments, the amplitudes and frequency of  $F_p^*$  were 2.0N and 1/30Hz.

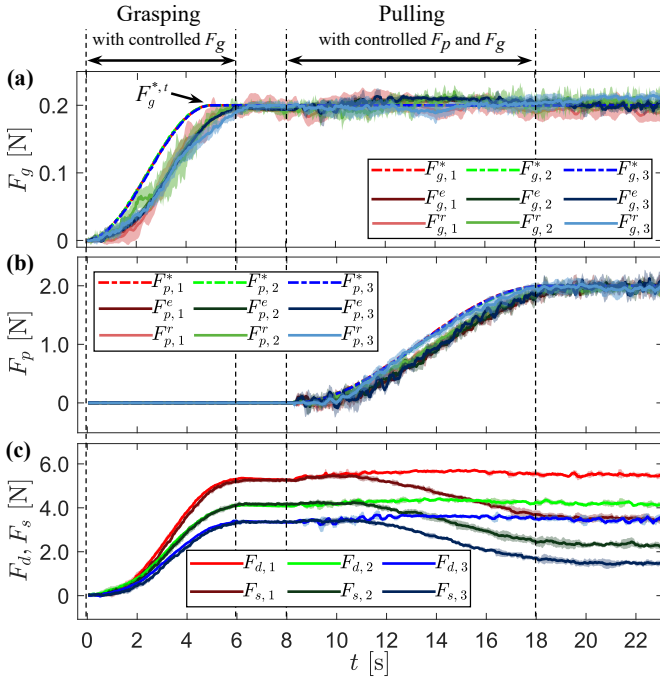


Fig. 8. Evaluation results of tissue traction with controlled  $F_g$  and  $F_p$ . (a) and (b) Comparisons of grasping force  $F_g$  and pulling force  $F_p$  results.  $F_{g,i}^r$  and  $F_{p,i}^r$  are measured reference forces,  $F_{g,i}^e$  and  $F_{p,i}^e$  indicate the estimated forces,  $F_{g,i}^*$  and  $F_{p,i}^*$  are targeted forces, and  $F_{g,i}^{*,t}$  (0.2N for all experiments) is the threshold targeted force for grasping.  $i \in \{1, 2, 3\}$  denotes experiment conducted with grasping angle  $\theta = 10^\circ, 30^\circ$ , and  $50^\circ$ . (c) Variations of driving force  $F_d$  and spring elastic force  $F_s$  during these experiments.

grasping phase (0–5s). Then, it kept constant during the pulling phase (8–18s) when the target pulling force  $F_p^*$  increased from 0 to 2.0N. Finally, both  $F_g^*$  and  $F_p^*$  kept constant during (18–25s). During (5–8s),  $F_g^*$  and  $F_p^*$  were constant to visually separate the grasping and pulling phases. Each experimental procedure was repeated five times.

The standard deviation plots Fig. 8(a) and (b) show the comparison of estimated, targeted, and reference values of  $F_g$  and  $F_p$ , respectively. Since all the experiments followed the same  $F_g^*$  and  $F_p^*$  profiles, their results almost overlaid. In these traction experiments, we are more concerned with the force variations during the pulling process, and Table I lists the worst-case errors (see Appendix-A) of  $F_g$  and  $F_p$  during

TABLE I  
ERRORS IN THE PULLING PHASE OF SIMULTANEOUS MULTIPLE FORCE CONTROL

Force	Comparison	Error	10°	30°	50°
$F_g$ [N]	$(F_g^*, F_g^e)$	Mean	0.0054	0.0071	0.0106
		RMS	0.0063	0.0083	0.0128
		Max	0.0151	0.0202	0.0377
	$(F_g^e, F_g^r)$	Mean	0.0144	0.0140	0.0171
		RMS	0.0163	0.0167	0.0201
		Max	0.0345	0.0448	0.0532
$F_p$ [N]	$(F_p^*, F_p^e)$	Mean	0.2480	0.2024	0.2019
		RMS	0.2890	0.2457	0.2385
		Max	0.5529	0.5382	0.5218
	$(F_p^e, F_p^r)$	Mean	0.1043	0.1122	0.1920
		RMS	0.1226	0.1331	0.2253
		Max	0.3068	0.3374	0.4437

this period.

We can see the mean, RMS, and maximum errors between  $F_g^*$  and  $F_g^e$  are all under (0.0106, 0.0128, 0.0377)N, which were comparable with that of experiments shown in Fig. 5. The mean, root mean square (RMS), and maximum errors between  $F_p^*$  and  $F_p^e$  are all under (0.2480, 0.2890, 0.5529)N, which were also comparable with that in experiments shown in Fig. 6. Moreover, compared to that without controlled grasping force (see Fig. 7), the maximum deviation of  $F_g$  in the pulling phase reduced by around 300% for  $\theta = 50^\circ$  (from 0.116N to 0.0377N), 470% for  $\theta = 30^\circ$  (from 0.096N to 0.0202N), 460% for  $\theta = 10^\circ$  (from 0.073N to 0.0151N). These indicate that simultaneous  $F_p$  and  $F_g$  control can be effectively achieved during the pulling process.

In addition, Fig. 8(c) shows the corresponding driving force  $F_d$  and spring elastic force  $F_s$  of these experiments. we can see less  $F_d$  and  $F_s$  were required for forceps with larger  $\theta$  to achieve the same  $F_{g,i}^{*,t}$ . Moreover, the driving force  $F_d$  remained nearly constant during the pulling phase while the spring elastic force  $F_s$  (equal to the supporting force) gradually decreased. This was because the constant grasping force required constant driving force, and the system had to reduce the elastic force  $F_s$  to ensure the increased pulling force  $F_p$ . This phenomenon confirmed the analysis in (16) and revealed that the decoupling control of  $F_g$  and  $F_p$  was achieved by indirectly controlling  $F_d$  and  $F_s$ .

#### IV. AUTOMATIC TRACTION-ASSISTED TISSUE RESECTION

Tissue traction is frequently performed in surgical operations such as lesion sampling and tumour dissection. Here, we demonstrate the feasibility of the proposed method for automatic tissue traction in a dual-arm tissue resection task on *ex vivo* tissues.

##### A. Experimental Setup and Operation Flow

1) *Experimental Setup*: Fig. 9(a) shows the experimental setup, where two UR robotic arms were adopted as the macro-level actuators. The *ex vivo* chicken tissue was placed in a human body phantom to simulate the lesion, and instruments were implemented through simulated minimally invasive ports on the phantom. The operator could supervise

the procedure and input orders through a designed graphic user interface (GUI), shown in Fig. 9(a), which also presents the sensed multiple forces, pulling distance, endoscopy image, and sensing-module camera frame in real-time. Both universal robotic arms, UR-1 and UR-2, have been pre-docked to the initial state, and the micro-level actuators were responsible for performing the automatic traction-assisted tissue resection task locally. Specifically, UR-1, carrying the forceps for tissue traction, was locked during the operation, while UR-2 was teleoperated by a touch device (3D Systems, USA) to adjust the pose of the scissors for tissue cutting.

To integrate the force controller and the robotic controller, we further designed a software architecture, as depicted in Fig. 9(b). The remote controller consists of the touch device and the laptop with GUI. The touch device was running on ROS melodic to teleoperate the robotic arm UR-1. The laptop was responsible for the operation flow, a Dell Latitude 5420 with i5-11<sup>th</sup> @ 2.6GHz cup, which communicated with the local controller through a serial port to receive the task state and send the commands. The local controller, an STM32H7 microcontroller, also contained two sub-controllers (a cutting controller and a force controller) and a state estimator. The force controller generated the inputs  $\mathbf{u} = [{}^R\dot{d}_l, {}^L\dot{d}_u]^\top$  and sent to the forceps' micro-level actuator. The cutting controller was responsible for controlling the scissors' actuator according to the received commands from the remote controller.

2) *Resection with Automatic Tissue Traction*: For typical tissue resection, we noticed that the required pulling force at the first cut is more significant than that of the following cuts. Therefore, the targeted pulling force  $F_p^*$  should be reduced after each cut. Moreover, because of the elasticity, the tissue body tends to collapse after the connection part has been cut out. This indicates the cutting surface may passively be revealed by the tissue collapse when the tissue has been pulled up to a certain displacement.

Considering the above phenomena and patterning after the clinical dissection procedure [17], we designed an operation flow with automatic traction. The automatic traction was built upon predefined grasping and pulling forces profiles, complemented by the pulling distance information. The forceps first reached the tissue with touch detection by comparing the estimated  $F_p$  with a set threshold  $F_p^{*,t} = -0.05\text{N}$ . Next, the tissue was grasped to the target grasping force  $F_g^* = 0.3\text{N}$  followed by pulling up and holding with an initial target pulling force  $F_p^{*,0} = 0.25\text{N}$ . After the pulling, the scissors were teleoperated to the target tissue, and cutting was performed. Then, the operation alternated between pulling and cutting several times, and the target pulling force  $F_p^{*,i}$  reduced to  $\rho F_p^{*,i-1}$  after  $i^{\text{th}}$  cut.  $i \in [1, m]$ ,  $m$  was the number of cuts performed, and  $\rho = 0.8$  was the reduction ratio. The incremental pulling distance  $\Delta d_p$  was limited by a threshold  $\Delta d_p^t = 20\text{mm}$ , and the total pulling distance  $d_p$  was limited by  $d_p^t = 30\text{mm}$ . A threshold for cut-off detection  $F_p^{*,c} = 0.05\text{N}$  was also included. When the estimated pulling force  $F_p^e$  after each cut was less than  $F_p^{*,c}$ , the forceps would not pull up the tissue further. Then, the operator was required to check whether the tissue had been cut off and confirm whether another cut was needed or could be moved out directly. The above operation flow is

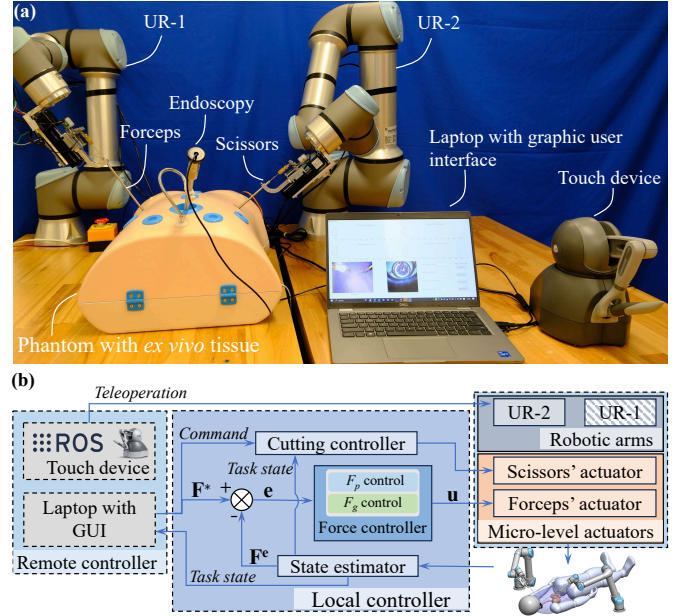


Fig. 9. (a) Experimental setup of robotic *ex vivo* tissue resections with automatic traction. A human body phantom was used for placing *ex vivo* chicken tissue simulating lesions. The micro-level actuators with instruments were mounted on two universal robotic arms, UR-1 and UR-2. Specifically, UR-1, carrying the forceps tissue grasping and pulling, was hocked to the initial pose and locked during the tissue resection procedure, while UR-2 was teleoperated by a touch device to adjust the pose of the scissors for tissue cutting. The instruments and endoscopy were implemented through simulated minimally invasive surgical ports on the phantom. The laptop provided the operator a graphic user interface (GUI) to monitor the procedure and input orders. (b) Integrated controller diagram of the dual-arm robotic system.

also summarized in Appendix-B.

## B. Tissue Resection Results

Here, the automatic tissue grasping process was achieved by (12) and (13), and the pulling process relied on (15) and (13). We conducted four resections, and their results are shown in Fig. 10(a), (b), (c), and (d), including grasping force  $F_g$ , pulling force  $F_p$ , and pulling distance  $d_p$ . The critical snapshots of the experimental procedure are also presented at the top of Fig. 10.

Four procedures were carried out with the same piece of tissue, but the localized conditions of the grasped tissues differed, and the scissors pose was teleoperated. As a result, the number of cuts ( $m$ ) performed and the operation time ( $t$ ) varied among these procedures. Specifically, for the experiments presented in Fig. 10(a), (b), and (d), four cuts were performed ( $m = 4$ ), while for the experiment in Fig. 10(c), five cuts were performed ( $m = 5$ ), as indicated by  $C_i$ . The rapid variations in pulling force  $F_p$  resulted from interactions between scissors and tissue. All procedures successfully cut the tissue off, indicating that automatic tissue traction with multi-force control is effectively implemented and has the potential to promote autonomous MIS.

## V. DISCUSSION

### A. Force Sensing and Tracking

1) *Sensing Resolution and Range*: Although through the distributed software framework design and direct memory ac-

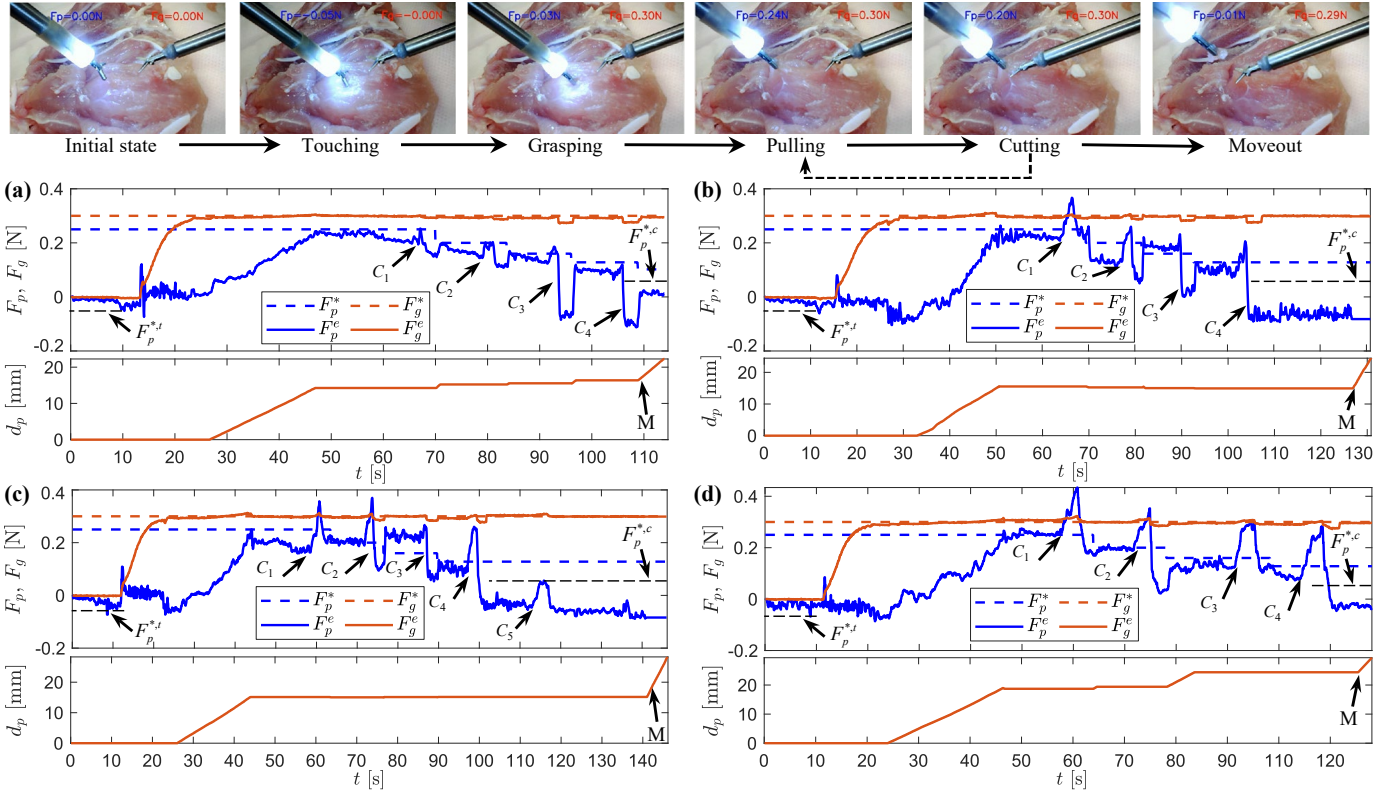


Fig. 10. Results of automatic traction-assisted tissue resections, where the top endoscopy snapshots show the critical stages of the operation flow. (a), (b), (c), and (d) present the results of four procedures, wherein  $F_g$ ,  $F_p$ , and  $d_p$  denote the grasping force, pulling force and pulling distance, respectively. Four procedures followed the same operation flow, wherein the forceps performed automatically, while the scissors relied on teleoperation to adjust each cut's pose. The forceps first reached the tissue with touching detection by comparing the estimated  $F_p$  with the set threshold  $F_p^{*,i} = -0.05\text{N}$ . Next, the tissue was grasped to the target grasping force  $F_g^* = 0.3\text{N}$  followed by pulled up to an initial target pulling force  $F_p^{*,0} = 0.25\text{N}$  and cut out by the scissors. Then, the operation alternated between pulling and cutting, and the target pulling force  $F_p^{*,i}$  ( $i \in [1, m]$ ) reduced to  $\rho F_p^{*,i-1}$  after  $i$ -th cutting.  $\rho$  was 0.8 and  $m$  (equaled 4 in (a), (b), and (d), and 5 in (c)) was the number of cuts ( $C_i$ ) performed. The incremental pulling distance  $\Delta d_p$  for each pulling action was limited by a threshold  $\Delta d_p^* = 20\text{mm}$ , and the total pulling distance  $d_p$  was limited by  $d_p^* = 30\text{mm}$ .  $F_p^{*,c} = 0.05\text{N}$  was a threshold for cut-off detection. When the estimated pulling force  $F_p^e$  after each cut was less than  $F_p^{*,c}$ , the forceps would not pull up the tissue further. The operator was required to check whether the tissue had been cut off and confirm whether another cut was required or if it could be directly moved out (denoted by M).

cess (DMA) communication, the local controller could achieve high-frequency operation with minimized signal interference, the updating frequency of estimated elastic supporting force  $F_s$  was limited to 30Hz by the camera (OVM6946, Omnivision Inc., USA) update rate. The frequency could be improved by adopting a camera with a higher rate. Consequently, the performance of force estimation and control could be further improved. Replacing the spring to a flexure with different stiffness, the sensitivity and resolution of the sensing module can also be configured. Additionally, the grasping force  $F_g$  estimation is related to the supporting force  $F_s$ , and the sensible range of  $F_s$  (limited by the spring's deformation) is  $[0 - 5]\text{N}$  in our prototype. Therefore, the sensible range of  $F_g$  is also limited and positively related to grasping angle  $\theta$ .

2) *Force Tracking*: We demonstrated the system has the ability to track force profiles with different frequencies and amplitude, as shown in Fig. 5, Fig. 6, and Fig. 8. Because the actuators' displacements and speeds can not change rapidly, the response speed of force control is limited, and there is a delay for the system to track the target force. For example, using the experimental setup shown in Fig. 4, we verified the

system's step response and the results are shown in Fig. 11. For target pulling force  $F_p^*$  with a 1.0N step signal, a 0.5s delay was observed in force tracking, while for target grasping force  $F_g^*$  with 0.35N step signal, a 1.5s delay was observed. However, the force variation in tissue traction often involves considerable tissue deformation, and no rapidly changed force is required [17]. Therefore, we believe this delay will not compromise the efficiency in tissue grasping and pulling, as demonstrated in Fig. 10.

### B. Automatic Traction in Ex vivo Tissue Resections

The tissue traction strategy proposed in Section IV seems straightforward, however, we still observed some inspiring phenomena by comparing and analyzing these results. From Fig. 10, we can see that for the same target pulling force  $F_p^{*,i}$ , the required pulling distance  $d_p$  varied. Specifically,  $d_p$  almost kept constant in Fig. 10(b) and (c), while it gradually increased in Fig. 10(a) and (d). This indicates that tissue pulling that solely relies on  $d_p$  has a higher potential to result in tissue split due to excessive pulling forces. On the other hand, we must admit that tissue split cannot be avoided by simply relying

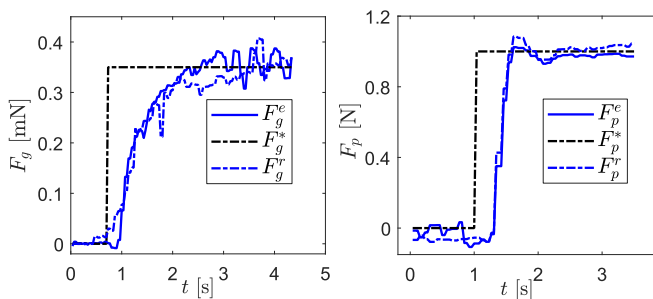


Fig. 11. Force tracking performance of step signal input.  $F_g^r$  and  $F_p^r$  are measured reference forces,  $F_g^e$  and  $F_p^e$  indicate the estimated forces.  $F_g^* = 0.35\text{N}$  and  $F_p^* = 1.0\text{N}$  are inputted step-signal target forces.

on the pulling force information either. This is because when tissue has been cut very finely, the pulling force exerted on the forceps will be too subtle to be reliably sensed and controlled. That is why incremental and total pulling distances should be limited in tissue traction and the operator was required to check the tissue condition when the pulling force  $F_p^e$  was less than  $F_p^{*,c} = 0.05\text{N}$ . We believe this tissue condition-checking task also has the potential to be automated with more input information, for example, the fluorescence of tumour [33].

We also conducted tissue traction with the grasping process achieved by (12) and (13), and the pulling process relied on (15) and (14), i.e., the grasping force  $F_g$  is not controlled during the pulling process. The tissue also has been successfully cut off, and the result is shown in Fig. 12. Since the required  $F_p$  in the tissue-pulling process is small (0.25N in these experiments), the force coupling was not obviously observed. However, another interesting phenomenon caught our attention: the grasping force  $F_g$  in Fig. 12 gradually decreased (0.04N reduction at the end, 12% of 0.3N) after each cut. This could result from the interaction between the scissors and tissue, which caused rapid force variation and impaired the grasping condition. This reduced grasping force could increase the risk of tissue slides in the following operations.

Nevertheless, the grasping force  $F_g$  in the experiments presented in Fig. 10 recovered to the target value  $F_g^*$  (with 0.003N errors at the end, 1% of 0.3N). Compared to the experiment in Fig. 12 that has a 12% reduction of  $F_g$ , enabling grasping force control in the pulling process could reduce tissue slid risk. This phenomenon further supports the criticality of simultaneous multi-force control in tissue manipulations.

The used parameters, including touch detection threshold  $F_p^{*,t}$ , targeted grasping force  $F_g^*$ , initial targeted pulling force  $F_p^*$ , reduction ratio  $\rho$ , pulling distance incremental threshold  $\Delta d_p^t$ , total pulling distance threshold  $d_p^t$ , and cutoff detection threshold  $F_p^{*,c}$ , were roughly chosen in experiments presented in Fig. 10 and Fig. 12. For more precise operation, these parameters should be identified according to clinical requirements. In practical surgery, external sensing modules, such as a vision system, could also provide more information for decision-making. Associating with additional information and considerations of clinical constraints, the strategy could potentially be extended to more general operations.

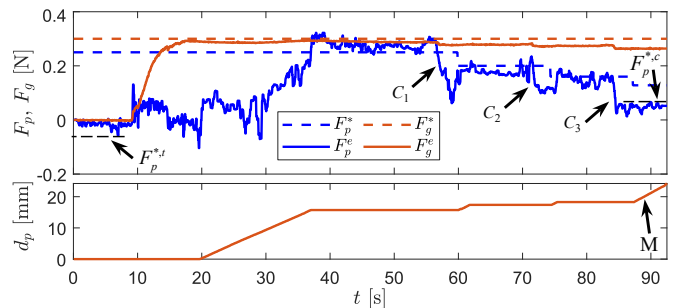


Fig. 12. Result of tissue resection, wherein the grasping force was not controlled during the pulling process.  $F_g$ ,  $F_p$ , and  $d_p$  are grasping force, pulling force and pulling distance results. The grasping force in this procedure gradually decreased due to instrument interactions (between scissors and tissue). The number of performed cuts (C) is three, each cut is indicated by  $C_i$ , and the tissue move-out by M.

### C. Other Applications

This paper demonstrated the potential application of multi-force control for automatic grasping and pulling by forceps through robotic tissue resection. The proposed force controller has the potential to be extended to other surgical operations as well. These include but are not limited to robotic palpation and tissue handling compensating for external motion disturbances. Considering the clinical constraints, these extended characteristics will be further studied in our future work with other tissue manipulation tasks.

Because the grasping force and pulling force can be controlled solely and simultaneously, more alternatives are provided to the operator for different applications. Moreover, with the one-step-docking design, the instrument can be replaced and delivered quickly. Specifically, the scissors and forceps were actuated by the same micro-level actuator in our prototype, as shown in Fig. 9(a). This could also bring benefits to sterilization and interoperative instrument exchanges.

## VI. CONCLUSION

This paper has introduced a method for automating tissue traction with micro-sized forceps featuring controlled grasping and pulling forces. Specifically, the grasping stage relied on a controlled grasping force, while the pulling stage was under the guidance of a controlled pulling force. In particular, during the pulling process, the simultaneous control of both grasping and pulling forces was also enabled for more precise tissue traction, achieved through force decoupling. The force controller was built upon a static model of tissue manipulation considering the interaction between the haptics-enabled forceps and soft tissue. The efficacy of this force control approach was validated through a series of experiments comparing targeted, estimated, and actual reference forces. Various tissue resections were conducted on *ex vivo* tissues employing a dual-arm robotic setup to verify the feasibility of the proposed method in surgical applications. Finally, we discussed the benefits of multi-force control in tissue traction, evidenced through comparative analyses of various *ex vivo* tissue resections. The results affirmed the feasibility of automatic tissue traction using micro-sized forceps with multi-force control, suggesting its potential to promote autonomous MIS. In the

future, this approach will be extended to accommodate other tissue manipulations and take into account more strict clinical constraints and surgical versatility.

## APPENDIX

### A. Worst-Case Error Calculation

The worst-case errors in Table I were calculated by

$$\left\{ \begin{array}{l} \text{Mean}(F_{\bullet}^*, F_{\bullet}^e) = \max(\text{mean}(F_{\bullet,i,j}^*, F_{\bullet,i,j}^e)) \\ \text{Mean}(F_{\bullet}^e, F_{\bullet}^r) = \max(\text{mean}(F_{\bullet,i,j}^e, F_{\bullet,i,j}^r)) \\ \text{RMS}(F_{\bullet}^*, F_{\bullet}^e) = \max(\text{rmse}(F_{\bullet,i,j}^*, F_{\bullet,i,j}^e)) \\ \text{RMS}(F_{\bullet}^e, F_{\bullet}^r) = \max(\text{rmse}(F_{\bullet,i,j}^e, F_{\bullet,i,j}^r)) \\ \text{Max}(F_{\bullet}^*, F_{\bullet}^r) = \max(\max(F_{\bullet,i,j}^*, F_{\bullet,i,j}^r)) \\ \text{Max}(F_{\bullet}^e, F_{\bullet}^r) = \max(\max(F_{\bullet,i,j}^e, F_{\bullet,i,j}^r)) \end{array} \right. ,$$

where  $i \in (1, 2, 3)$  denotes different  $\theta = (10^\circ, 30^\circ, 50^\circ)$ ,  $j \in (1, 2, 3, 4, 5)$  is the index of the five repeated experiments, and  $\bullet$  denotes subscript  $\{g, p\}$  for grasping and pulling forces, respectively.

### B. Tissue Resection Operation Flow

Tissue resection operation flow of experiments conducted in Fig. 10 and Fig. 12

---

#### Algorithm 1 Tissue Resection Operation Flow

---

**Input:**  $F_g^*, F_p^{*,0}, \rho, \Delta d_p^t, d_p^t$ , and  $F_p^{*,c}$

- 1: **while**  $F_p \geq F_p^{*,t}$  **do** // Touch detection
- 2:   move forceps forward;
- 3: **end while**
- 4: **while**  $F_g \leq F_g^*$  **do** // Tissue grasping
- 5:   grasp tissue with (12) and (13);
- 6: **end while**
- 7: **while**  $F_p \leq F_p^{*,0}$  **do** // Tissue pulling
- 8:   pull tissue with (15) and (13); // Exps in Fig. 10
- 9:   // pull tissue with (15) and (14); // Exp in Fig. 12
- 10: **end while**
- 11: **while**  $F_p \geq F_p^{*,c}$  **do** // Tissue cutting and pulling
- 12:   cut tissue with scissors;
- 13:    $i = i + 1$ ;
- 14:    $F_p^{*,i} = \rho F_p^{*,i-1}$ ;
- 15:   **while**  $F_p \leq F_p^{*,i}$  and  $d_p \leq d_p^t$  **do**
- 16:     **while**  $\Delta d_p \leq \Delta d_p^t$  **do**
- 17:       pull tissue with (15) and (13); // Exps in Fig. 10
- 18:       // pull tissue with (15) and (14); // Exp in Fig. 12
- 19:     **end while**
- 20:   **end while**
- 21: **end while**
- 22: final operator check and cut tissue if required;
- 23: move out the cut-off tissue;

---

## REFERENCES

- [1] G.-Z. Yang, J. Bellingham, P. E. Dupont, P. Fischer, L. Floridi, R. Full, N. Jacobstein, V. Kumar, M. McNutt, R. Merrifield *et al.*, "The grand challenges of science robotics," *Science robotics*, vol. 3, no. 14, p. eaar7650, 2018.
- [2] P. E. Dupont, B. J. Nelson, M. Goldfarb, B. Hannaford, A. Menciassi, M. K. O'Malley, N. Simaan, P. Valdastri, and G.-Z. Yang, "A decade retrospective of medical robotics research from 2010 to 2020," *Science Robotics*, vol. 6, no. 60, p. eabi8017, 2021.
- [3] P. E. Dupont, N. Simaan, H. Choset, and C. Rucker, "Continuum robots for medical interventions," *Proceedings of the IEEE*, vol. 110, no. 7, pp. 847–870, 2022.
- [4] A. Razjigaev, A. K. Pandey, D. Howard, J. Roberts, and L. Wu, "End-to-end design of bespoke, dexterous snake-like surgical robots: A case study with the raven ii," *IEEE Transactions on Robotics*, vol. 38, no. 5, pp. 2827–2840, 2022.
- [5] C. J. Nwafor, C. Girerd, G. J. Laurent, T. K. Morimoto, and K. Rabenoroosa, "Design and fabrication of concentric tube robots: A survey," *IEEE Transactions on Robotics*, 2023.
- [6] L. Wu, S. Song, K. Wu, C. M. Lim, and H. Ren, "Development of a compact continuum tubular robotic system for nasopharyngeal biopsy," *Medical & biological engineering & computing*, vol. 55, pp. 403–417, 2017.
- [7] J. Wang, C. Hu, G. Ning, L. Ma, X. Zhang, and H. Liao, "A novel miniature spring-based continuum manipulator for minimally invasive surgery: Design and evaluation," *IEEE/ASME Transactions on Mechatronics*, 2023.
- [8] Z. Hu, J. Li, and S. Wang, "Design and kinematics of a robotic instrument for natural orifice transluminal endoscopic surgery," *IEEE/ASME Transactions on Mechatronics*, 2023.
- [9] K. Price, J. Peine, M. Mencattelli, Y. Chitalia, D. Pu, T. Looi, S. Stone, J. Drake, and P. E. Dupont, "Using robotics to move a neurosurgeon's hands to the tip of their endoscope," *Science Robotics*, vol. 8, no. 82, p. eadg6042, 2023.
- [10] H. Gao, X. Yang, X. Xiao, X. Zhu, T. Zhang, C. Hou, H. Liu, M. Q.-H. Meng, L. Sun, X. Zuo *et al.*, "Transendoscopic flexible parallel continuum robotic mechanism for bimanual endoscopic sub-mucosal dissection," *The International Journal of Robotics Research*, p. 02783649231209338, 2023.
- [11] L. Wu, F. Yu, T. N. Do, and J. Wang, "Camera frame misalignment in a teleoperated eye-in-hand robot: Effects and a simple correction method," *IEEE Transactions on Human-Machine Systems*, vol. 53, no. 1, pp. 2–12, 2022.
- [12] Y. Kong, S. Song, N. Zhang, J. Wang, and B. Li, "Design and kinematic modeling of in-situ torsionally-steerable flexible surgical robots," *IEEE Robotics and Automation Letters*, vol. 7, no. 2, pp. 1864–1871, 2022.
- [13] H. Yu, L. Wu, K. Wu, and H. Ren, "Development of a multi-channel concentric tube robotic system with active vision for transnasal nasopharyngeal carcinoma procedures," *IEEE Robotics and Automation Letters*, vol. 1, no. 2, pp. 1172–1178, 2016.
- [14] Z. Li, X. Li, J. Lin, D. Yang, J. Xu, S. Zhang, and J. Guo, "Design and application of multi-dimensional force/torque sensors in surgical robots: A review," *IEEE Sensors Journal*, 2023.
- [15] O. A. Van der Meijden and M. P. Schijven, "The value of haptic feedback in conventional and robot-assisted minimal invasive surgery and virtual reality training: a current review," *Surgical endoscopy*, vol. 23, pp. 1180–1190, 2009.
- [16] A. Abiri, J. Pensa, A. Tao, J. Ma, Y.-Y. Juo, S. J. Askari, J. Bisley, J. Rosen, E. P. Dutton, and W. S. Grundfest, "Multi-modal haptic feedback for grip force reduction in robotic surgery," *Scientific reports*, vol. 9, no. 1, p. 5016, 2019.
- [17] J. E. Skandalakis, P. N. Skandalakis, and L. J. Skandalakis, "Thyroglossal duct cystectomy," in *Surgical anatomy and technique*. Springer, 2021, pp. 69–72.
- [18] Z. Liu, Z. Liao, D. Wang, C. Wang, C. Song, H. Li, and Y. Liu, "Recent advances in soft biological tissue manipulating technologies," *Chinese Journal of Mechanical Engineering*, vol. 35, no. 1, pp. 1–34, 2022.
- [19] U. Kim, Y. B. Kim, J. So, D.-Y. Seok, and H. R. Choi, "Sensorized surgical forceps for robotic-assisted minimally invasive surgery," *IEEE Transactions on Industrial Electronics*, vol. 65, no. 12, pp. 9604–9613, 2018.
- [20] D.-Y. Seok, Y. B. Kim, U. Kim, S. Y. Lee, and H. R. Choi, "Compensation of environmental influences on sensorized-forceps for practical surgical tasks," *IEEE Robotics and Automation Letters*, vol. 4, no. 2, pp. 2031–2037, 2019.
- [21] T. Liu, T. Zhang, J. Katupitiya, J. Wang, and L. Wu, "Haptics-enabled forceps with multimodal force sensing: Toward task-autonomous surgery," *IEEE/ASME Transactions on Mechatronics*, pp. 1–12, 2023.
- [22] A. A. Nazari, F. Janabi-Sharifi, and K. Zareinia, "Image-based force estimation in medical applications: A review," *IEEE Sensors Journal*, vol. 21, no. 7, pp. 8805–8830, 2021.

- [23] N. Haouchine, W. Kuang, S. Cotin, and M. Yip, "Vision-based force feedback estimation for robot-assisted surgery using instrument-constrained biomechanical three-dimensional maps," *IEEE Robotics and Automation Letters*, vol. 3, no. 3, pp. 2160–2165, 2018.
- [24] D.-H. Lee, W. Hwang, and S.-C. Lim, "Interaction force estimation using camera and electrical current without force/torque sensor," *IEEE Sensors Journal*, vol. 18, no. 21, pp. 8863–8872, 2018.
- [25] E. Nwoye, W. L. Woo, B. Gao, and T. Anyanwu, "Artificial intelligence for emerging technology in surgery: Systematic review and validation," *IEEE Reviews in Biomedical Engineering*, 2022.
- [26] K. L. Johnson and K. L. Johnson, *Contact mechanics*. Cambridge university press, 1987.
- [27] P. Xiang, J. Zhang, D. Sun, K. Qiu, Q. Fang, X. Mi, Y. Wang, R. Xiong, and H. Lu, "Learning-based high-precision force estimation and compliant control for small-scale continuum robot," *IEEE Transactions on Automation Science and Engineering*, 2023.
- [28] L. Wijayarathne, Z. Zhou, Y. Zhao, and F. L. Hammond, "Real-time deformable-contact-aware model predictive control for force-modulated manipulation," *IEEE Transactions on Robotics*, 2023.
- [29] Q. Sheng, Z. Geng, L. Hua, and X. Sheng, "Hybrid vision-force robot force control for tasks on soft tissues," in *2021 27th International Conference on Mechatronics and Machine Vision in Practice (M2VIP)*. IEEE, 2021, pp. 705–710.
- [30] P. S. Zarrin, A. Escoto, R. Xu, R. V. Patel, M. D. Naish, and A. L. Trejos, "Development of a 2-dof sensorized surgical grasper for grasping and axial force measurements," *IEEE Sensors Journal*, vol. 18, no. 7, pp. 2816–2826, 2018.
- [31] W. Lai, L. Cao, J. Liu, S. C. Tjin, and S. J. Phee, "A three-axial force sensor based on fiber bragg gratings for surgical robots," *IEEE/ASME Transactions on Mechatronics*, vol. 27, no. 2, pp. 777–789, 2021.
- [32] Y. Li, F. Richter, J. Lu, E. K. Funk, R. K. Orosco, J. Zhu, and M. C. Yip, "Super: A surgical perception framework for endoscopic tissue manipulation with surgical robotics," *IEEE Robotics and Automation Letters*, vol. 5, no. 2, pp. 2294–2301, 2020.
- [33] Y. Woo, S. Chaurasiya, M. O'Leary, E. Han, and Y. Fong, "Fluorescent imaging for cancer therapy and cancer gene therapy," *Molecular Therapy-Oncolytics*, vol. 23, pp. 231–238, 2021.



**Jay Katupitiya** received the B.S. degree in production engineering from the University of Peradeniya, Peradeniya, Sri Lankain, in 1978, and the Ph.D. degree in mechanical engineering from the Katholieke Universiteit Leuven, Leuven, Belgium, in 1985. He is currently an Associate Professor with the University of New South Wales, Sydney, NSW, Australia. His main research interest includes the development of sophisticated control methodologies for the precision guidance of field vehicles on rough terrain at high speeds.



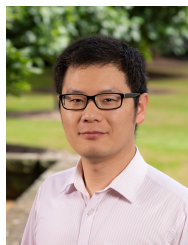
**Jiaole Wang** received the B.E. degree in mechanical engineering from Beijing Information Science and Technology University, Beijing, China, in 2007, the M.E. degree in human & artificial intelligent systems from the Department of Human and Artificial Intelligent Systems, University of Fukui, Fukui, Japan, in 2010, and the Ph.D. degree in electronic engineering from the Department of Electronic Engineering, The Chinese University of Hong Kong (CUHK), Hong Kong, in 2016. He was a Research Fellow with Pediatric Cardiac Bioengineering Laboratory, Department of Cardiovascular Surgery, Boston Children's Hospital and Harvard Medical School, Boston, MA, USA. He is currently an Associate Professor with the School of Mechanical Engineering and Automation, Harbin Institute of Technology (Shenzhen), Shenzhen, China. His main research interests include medical and surgical robotics, image-guided surgery, human-robot interaction, and magnetic tracking and actuation for biomedical applications.



**Tangyou Liu** received the B.S. degree in mechanical engineering from the Southwest University of Science and Technology (SWUST), Mianyang, China, in 2017, and the M.S. degree in mechanical engineering, as an outstanding graduate, from the Harbin Institute of Technology, Shenzhen (HITSz), Shenzhen, China, in 2021, supervised by Prof. Max Q.-H. Meng. He is currently working toward the Ph.D. degree in mechatronic engineering with the University of New South Wales (UNSW), Sydney, NSW, Australia, under the supervision of Dr. Liao Wu. He was with KUKA, China, as a System Development Engineer. He was awarded the champion of the KUKA China R&D Innovation Challenge and the IEEE ICRA2023 Best Poster. His current research interests include medical and surgical robots.



**Xiaoyi Wang** received the B.E. degree and M.E. degree from Harbin Institute of Technology (HIT), Harbin, China in 2014 and 2017, respectively. Then, she received her Ph.D. degree from University of New South Wales (UNSW), Sydney, Australia, in 2022, where she is working as a postdoctoral research fellow. Her current research interests include the control of aerospace robots and medical robots, nonlinear control, and stochastic optimal control.



**Liao Wu** received the B.S. and Ph.D. degrees in mechanical engineering from Tsinghua University, Beijing, China, in 2008 and 2013, respectively. From 2014 to 2015, he was a Research Fellow with National University of Singapore, Singapore. From 2016 to 2018, he was a Vice-Chancellor's Research Fellow with Queensland University of Technology, Brisbane, Australia. From 2016 to 2020, he was with the Australian Centre for Robotic Vision, an ARC Centre of Excellence. He is currently a Senior Lecturer with the School of Mechanical and Manufacturing Engineering, University of New South Wales, Sydney, Australia. His research interests cover medical and industrial robotics, including flexible and intelligent surgical robot design, human-robot interaction, assistive robotics, and robot modeling and calibration.